

Title	Breaking Lorentz reciprocity to overcome the time-bandwidth limit in physics and engineering
Authors	Tsakmakidis, K. L.;Shen, L.;Schulz, Sebastian A.;Zheng, X.;Upham, J.;Deng, X.;Altug, H.;Vakakis, A. F.;Boyd, R. W.
Publication date	2017-06-23
Original Citation	Tsakmakidis, K. L., Shen, L., Schulz, S. A., Zheng, X., Upham, J., Deng, X. Altug, H., Vakakis, A. F. and Boyd, R. W. (2017) 'Breaking Lorentz reciprocity to overcome the time-bandwidth limit in physics and engineering', Science, 356(6344), pp. 1260-1264. doi:10.1126/science.aam6662
Type of publication	Article (peer-reviewed)
Link to publisher's version	10.1126/science.aam6662
Rights	© 2017, the Authors, some rights reserved; exclusive licensee American Association for the Advancement of Science.
Download date	2025-04-18 03:50:40
Item downloaded from	<a href="https://hdl.handle.net/10468/14963">https://hdl.handle.net/10468/14963</a>



[www.sciencemag.org/content/356/6344/1260/suppl/DC1](http://www.sciencemag.org/content/356/6344/1260/suppl/DC1)

## Supplementary Materials for

### **Breaking Lorentz reciprocity to overcome the time-bandwidth limit in physics and engineering**

K. L. Tsakmakidis,\* L. Shen, S. A. Schulz, X. Zheng, J. Upham, X. Deng, H. Altug,  
A. F. Vakakis, R. W. Boyd\*

\*Corresponding author. Email: [kostsakmakidis@gmail.com](mailto:kostsakmakidis@gmail.com) (K.L.T.);  
[rboyd@uottawa.ca](mailto:rboyd@uottawa.ca) (R.W.B.)

Published 23 June 2017, *Science* **356**, 1260 (2017)

DOI: [10.1126/science.aam6662](https://doi.org/10.1126/science.aam6662)

#### **This PDF file includes:**

Materials and Methods  
Figs. S1 to S3  
Table S1  
References

## Materials and Methods

### Bandwidth and lifetime characteristics of reciprocal and non-reciprocal devices

There are subtle but important differences between the (bandwidth, lifetime and  $Q$ -factor) characteristics of reciprocal and non-reciprocal devices, thus appropriate care should accordingly be exercised when analyzing the above characteristics of such devices.

Specifically, as shown in the first row of Table S1 below, the key property in a reciprocal device is that because of time-reversal invariance the rates of input and output of energy into/from the device are equal (17, 18),  $\rho_{\text{in}} = 2/\tau_{\text{in}} = \rho_{\text{out}} = 2/\tau_{\text{out}}$ , where the factor of ‘2’ arises because  $\rho_{\text{in}}$  and  $\rho_{\text{out}}$  refer to the energy (rather than the amplitude) rate (17). Furthermore, we normally operate in the underdamped regime, where energy can couple into the device before it dissipates, i.e.

$$2/\tau_{\text{in}} = 2/\tau_{\text{out}} \gg 2/\tau_0 \rightarrow \rho_{\text{in}} = \rho_{\text{out}} \gg 2/\tau_0 \quad (\text{S1})$$

with  $2/\tau_0$  being the energy-decay rate owing to internal, dissipative/Joule losses. With these notes in mind, we may use the well-known expression for the ‘loaded in-coupling  $Q$ ’,  $Q_{L,\text{in}}$  (17), summarized in the last row of Table S1 (Eq. (S3)), to calculate an approximate relation linking the in-coupling bandwidth  $\Delta\omega_{\text{in}}$  (i.e., the bandwidth available at the input port of the device) to the in-coupling rate  $\rho_{\text{in}}$ :

$$\frac{1}{Q_{L,\text{in}}} = \frac{\Delta\omega_{\text{in}}}{\omega_0} \xrightarrow{(\text{S3})} = \frac{2\pi/\tau_0}{\omega_0} + \frac{\pi\rho_{\text{in}}}{\omega_0} \xrightarrow{(\text{S1})} \boxed{\Delta\omega_{\text{in}} \approx \pi\rho_{\text{in}}}. \quad (\text{S2})$$

Reciprocal	Non-reciprocal
<p><b>One</b> bandwidth (<math>\Delta\omega_{\text{in}} = \Delta\omega_{\text{out}} = \Delta\omega</math>)</p> <p style="text-align: center;"><math>\Delta\omega_{\text{in}} = \pi\rho_{\text{in}}</math></p> <p style="text-align: center;"><math>\Delta\omega_{\text{out}} = \boxed{\pi\rho_{\text{out}} = \pi\rho_{\text{in}}} = \Delta\omega_{\text{in}}</math></p>	<p><b>Two</b> bandwidths (<math>\Delta\omega_{\text{in}} \neq \Delta\omega_{\text{out}}</math>)</p> <p style="text-align: center;"><math>\Delta\omega_{\text{in}} = \pi\rho_{\text{in}} \gg \pi\rho_{\text{out}} = \Delta\omega_{\text{out}}</math></p> <p style="text-align: center;"><math>\Delta\omega_{\text{out}} = 2\pi/\tau_0</math> (<math>\rho_{\text{out}} \rightarrow 0 \Rightarrow \tau_{\text{out}} \rightarrow \infty</math>)</p>
$\Delta\tau = \tau_{\text{out}} = \frac{2}{\rho_{\text{out}}} = \frac{2}{\rho_{\text{in}}} = \frac{2\pi}{\Delta\omega}$	$\Delta\tau = \tau_0 \neq \frac{2}{\rho_{\text{in}}} = \frac{2\pi}{\Delta\omega_{\text{in}}}$
$\frac{1}{Q_{L,\text{in}}} = \frac{1}{Q_0} + \frac{1}{Q_{\text{in}}} \quad (\text{S3})$	$\frac{1}{Q_{L,\text{in}}} = \frac{1}{Q_0} + \frac{1}{Q_{\text{in}}}$ $\frac{1}{Q_{L,\text{out}}} = \frac{1}{Q_0} + \frac{1}{Q_{\text{out}}}$

**Table S1.** Bandwidth, lifetime and  $Q$ -factor characteristics of reciprocal and non-reciprocal resonant devices.

The situation is drastically different in highly asymmetric, non-reciprocal devices where the in-coupling rate may be much larger than the out-coupling rate,  $\rho_{\text{in}} \gg \rho_{\text{out}}$ . In such a device, while the in-coupling bandwidth  $\Delta\omega_{\text{in}}$  is still proportional to the in-coupling rate,  $\Delta\omega_{\text{in}} \propto \rho_{\text{in}}$ , and can therefore be large, the out-coupling bandwidth  $\Delta\omega_{\text{out}}$  is proportional to the out-coupling rate,  $\Delta\omega_{\text{out}} \propto \rho_{\text{out}}$ , and for large asymmetry (as in the herein considered structure, in which the in-coupling rate is large but nothing can escape from the localization point at the rightmost end; see Fig. 2B) it can become zero,  $\Delta\omega_{\text{out}} \rightarrow 0$  ( $\Rightarrow \tau_{\text{out}} \rightarrow \infty$ ). Thus, in that case, the lifetime of the excitation  $\Delta\tau = 1/(1/\tau_0 + 1/\tau_{\text{out}})$  now

becomes equal to  $\tau_0$  ( $\Delta\tau \approx \tau_0$ ), as shown in the second row of Table S1 above, rather than equal to  $\tau_{\text{out}}$  as was the case for (the underdamped regime of) reciprocal devices. Importantly, in that case, the lifetime  $\Delta\tau$  (being equal to  $\tau_0$ ) is completely decoupled from the in-coupling rate and bandwidth, i.e.  $\Delta\tau \neq 2/\rho_{\text{in}} = 2\pi/\Delta\omega_{\text{in}}$ , simply because time-reversal symmetry linking  $\rho_{\text{in}}$  to  $\rho_{\text{out}}$  (see highlighted box in the first row of Table S1) is not valid anymore (as the system is non-reciprocal, i.e. Lorentz reciprocity is broken, e.g. by application of an external magnetic bias as in the heterostructure of Fig. 2B). By contrast, as inferred from the above discussion and as summarized in the left column of Table S1, for reciprocal devices it is always  $\Delta\tau = 2\pi/\Delta\omega_{\text{in}}$ , and hence the time-bandwidth product is always constant – or, generally, upper-limited. Since time invariance does not apply anymore in devices where Lorentz reciprocity is broken, and  $\Delta\tau \neq 2\pi/\Delta\omega_{\text{in}}$ , the time-bandwidth product may, now, in principle, take on arbitrarily large values – much higher than what was, until now, considered to be the ‘fundamental’ upper limit characterizing reciprocal resonant and waveguiding systems (which, as explained in the main text, is usually thought to ‘fundamentally’ arise from basic Fourier-transform considerations in the derivation of the frequency response of lossy resonators and guiding systems (1-5, 7, 9, 13-18)).

#### Parameters used in results/figures shown in the main text

In the attaining the band diagram of **Fig. 2C**, the following optogeometric parameters were used:

- Magnetized InSb:  $N_e = 1.1 \times 10^{16} \text{ cm}^{-3}$  (electron density) (23, 26);  $\epsilon_\infty = 15.6$ ;  $\omega_p = [(N_e e^2)/(\epsilon_\infty \epsilon_0 m^*)]^{1/2} = 4\pi \times 10^{12} \text{ rad/s}$  (effective plasma frequency);  $f_p = \omega_p/2\pi = 2 \text{ THz}$ ;  $B_0 = 0.2 \text{ T}$  (external magnetic field);  $\omega_c = eB_0/m^* = 0.2\omega_p$  (electron cyclotron frequency).
- Si layer:  $\epsilon_r = 11.68$ ;  $d = 0.08\lambda_p = 12 \text{ }\mu\text{m}$  ( $\lambda_p = c/f_p = 150 \text{ }\mu\text{m}$ ).
- Ag metal:  $\epsilon_{\text{Ag}} = 1 - \omega_{pe}^2/[\omega(\omega + i\omega_\tau)]$ , with  $\omega_{pe} = 1.367 \times 10^{16} \text{ rad/s}$  and  $\omega_\tau = 2.733 \times 10^{13} \text{ rad/s}$ .

For the simulation results of **Fig. 3**, the following parameters were used:

- Waveguide length:  $L = 800 \text{ }\mu\text{m}$ ; loss of InSb:  $\nu = 0.001\omega_p$ .
- Magnetic current line source:  $I_m(t) = \exp[-(t - t_0)^2/\tau^2] \exp(-i2\pi f_0 t)$ , where  $f_0 = 1.5 \text{ THz}$ ,  $t_0 = 15T_p$ ;  $\tau = 6.4T_p$  (with  $T_p = 2\pi/\omega_p = 0.5 \text{ ps}$ ), positioned  $100 \text{ }\mu\text{m}$  away from the leftmost end and  $6 \text{ }\mu\text{m}$  above the Si/InSb interface. The spectrum of the source is  $A(\omega) = A_0 \exp[-(f - f_0)^2/\Delta f^2]$ , with  $\Delta f = 0.1 \text{ THz}$  (FWHM =  $0.1665 \text{ THz}$ ).

For the simulation results of **Figs. 4A, B** (where  $\nu$  was variable) the used optogeometric parameters were the same as those used in Figs. 2 and 3, but with  $t_0 = 80T_p$ ,  $\tau = 31.8T_p$  and  $\Delta f = 0.02 \text{ THz}$ .

For the simulation results of **Figs. 4C, D** (where  $\omega_c$  or  $B_0$  were variable) the used optogeometric parameters were the same as those used in Figs. 2, 3, 4A, 4B.

### Dispersion relation (Eq. (6)) and FDTD simulations

To obtain the dispersion equation (Eq. (6)) in the main body of the paper, we assume that the excited surface magnetoplasmon (SMP) in the heterostructure of Fig. 2B is transverse magnetic (TM, or  $p$ -) polarized, with the nonzero component of the magnetic field,  $H_y$ , having the following spatio-temporal variation:

$$H_y(x, z) = [A_1 \exp(-\alpha_d x) + A_2 \exp(\alpha_d x)] \exp[i(kz - \omega t)], \text{ in the Si layer } (0 \leq x \leq d),$$

$$H_y(x, z) = B \exp(\alpha_s x) \exp[i(kz - \omega t)], \text{ in the semiconductor/InSb layer } (x \leq 0),$$

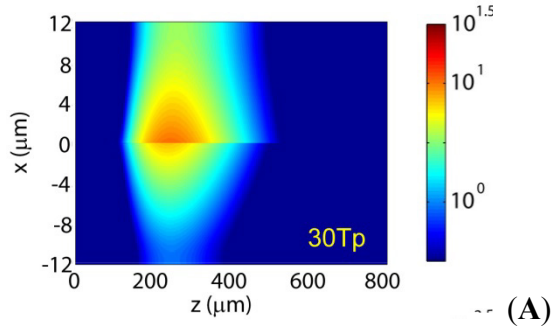
$$\text{and } H_y(x, z) = C \exp(-\alpha_m x) \exp[i(kz - \omega t)], \text{ in the upper metal/Ag } (x \geq 0),$$

where  $k$  is the longitudinal propagation constant, and the remaining parameters are defined in the main text. The  $E_z$  component can be obtained from the above expressions for  $H_y$ , as:  $E_z = [i/(\omega \epsilon)] \partial H_y / \partial x$ . Upon matching the two tangential field components at the Si/InSb and Ag/Si interfaces we immediately obtain the transcendental dispersion relation, Eq. (6), in the main text of the paper.

For the full-wave simulation results shown in Figs. 3 and 4 in the main text (and in Fig. S1 below), we used the finite-difference time-domain (FDTD) method. The relevant equations in the gyroelectric semiconductor (InSb) are then:

$$\begin{aligned} \frac{\partial E_y}{\partial x} - \frac{\partial E_x}{\partial y} &= -\mu_0 \frac{\partial H_z}{\partial t}, \\ \frac{\partial H_z}{\partial y} &= \epsilon_0 \epsilon_\infty \frac{\partial E_x}{\partial t} + (J_x^- + J_x^+) + i(J_y^- - J_y^+), \\ -\frac{\partial H_z}{\partial x} &= \epsilon_0 \epsilon_\infty \frac{\partial E_y}{\partial t} - i(J_x^- - J_x^+) + i(J_y^- + J_y^+), \\ \frac{\partial J_{x,y}^\pm}{\partial t} + (v \mp i\omega_c) J_{x,y}^\pm &= \frac{1}{2} \epsilon_0 \omega_p^2 E_{x,y}. \end{aligned} \quad (\text{S4a-d})$$

The magnetic current line source was of the form:  $I_m = \exp[-(t - t_0)^2 / \tau^2] \exp(-i2\pi f_0 t)$ ,  $t \geq 0$ , and was exciting a pulse whose bandwidth was in all cases within the ‘complete unidirectional propagation’ (CUP) region of the band-diagram (Fig. 2C). Figures S1(A)-(E) below illustrate successive snapshots from these time-domain simulations:



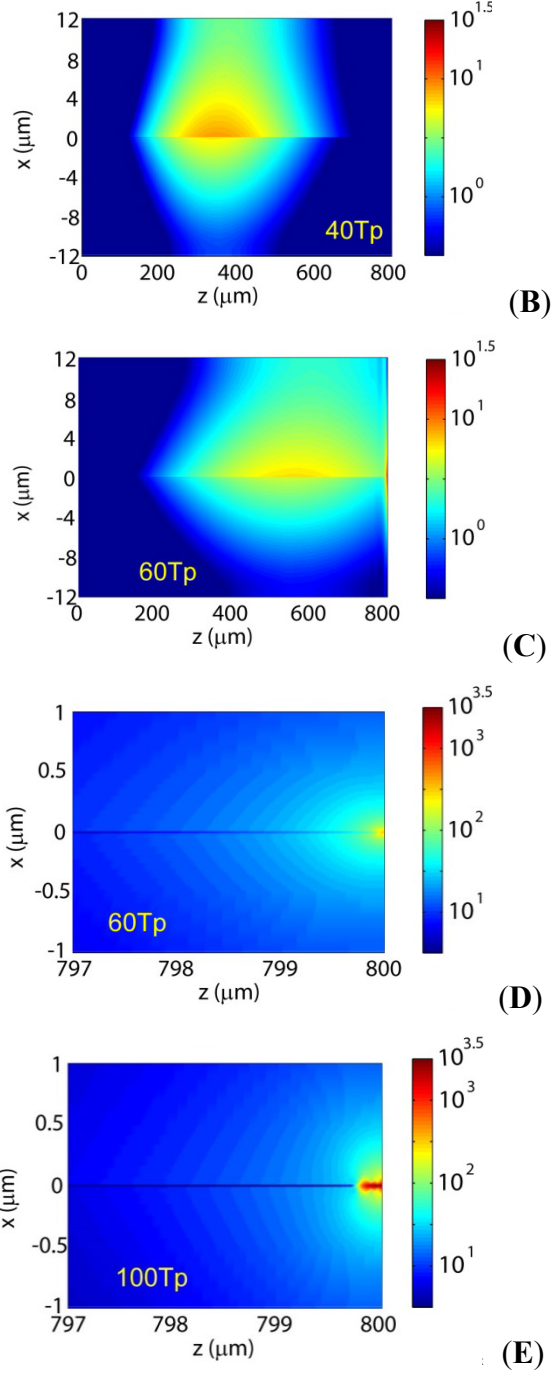


**Figure S1.** Propagation and trapping dynamics. Successive snapshots of the propagation of a surface magnetoplasmon along the gyroelectric semiconductor heterostructure of Fig. 2B, with its eventual localization (and thereafter absorption; not shown here) at the rightmost end. Shown here are the successive distributions of the E-field amplitude. Note the change of scale in the colorbar and in the horizontal axis in parts D and E, as compared with parts A-C.

In the FDTD simulations we used a uniform grid mesh with  $\Delta x = 0.1 \mu\text{m}$  and  $\Delta z = 0.5 \mu\text{m}$ , apart from the region close to the Si/InSb interface and the rightmost Si-InSb/Ag interfaces where a non-uniform mesh was used with  $\delta x = 1/128 \mu\text{m}$  and  $\delta z = 1/512 \mu\text{m}$

(otherwise, non-convergence or spurious back-reflections may be observed). Also, for the results of Fig. 3B we used a computational box of side length 4  $\mu\text{m}$ , located around the rightmost Si-InSb/Ag interfaces, to record the time evolution of the electromagnetic energy inside it (where, e.g., the energy density inside the dispersive semiconductor is given by  $U_s = (1/4)\mathbf{E}^* d(\omega\tilde{\epsilon}_{\text{InSb}})/d\omega\mathbf{E} + (1/4)\mu_0 |\mathbf{H}|^2$ ).

#### Derivation of Eq. (1) in the main text

Let us assume that the field amplitude  $\alpha$  inside a resonant system varies with time as  $\alpha(t) \propto \cos(\omega_0 t)e^{-(1/2)\Gamma t}$ , for  $t \geq 0$ . The Fourier transform of this expression reads:  $A(\omega) = (\Gamma/2 + i\omega)/[(\Gamma/2 + i\omega)^2 + \omega_0^2]$ . In the resonance approximation, we have (3):  $\omega_0^2 - \omega^2 = (\omega_0 + \omega)(\omega_0 - \omega) \approx 2\omega_0(\omega_0 - \omega) \approx 2\omega(\omega_0 - \omega)$ . Furthermore, in the underdamped regime mentioned above, we assume that  $\Gamma/2 \ll \omega_0$ . With these approximations in mind, we successively have for  $A(\omega)$ :

$$\begin{aligned} A(\omega) &= \frac{\Gamma/2 + i\omega_0}{2\omega_0} \frac{1}{\omega_0 - \omega + i\Gamma/2} \\ &= \frac{\omega_0 - i\Gamma/2}{\Gamma\omega_0} \frac{1}{1 - i[(\omega - \omega_0)/\Gamma/2]} \Rightarrow \\ I(\omega) \propto |A(\omega)|^2 &= \frac{\omega_0^2 + (\Gamma/2)^2}{(\Gamma\omega_0)^2} \frac{(\Gamma/2)^2}{(\omega - \omega_0)^2 + (\Gamma/2)^2}, \end{aligned} \quad (\text{S5})$$

which is Eq. (1) used in the main text.

#### Preservation of bandwidth during the static trapping and storage

In this linear, time-invariant system, the ‘‘bandwidth’’ is essentially the in-coupling bandwidth  $\Delta\omega_{\text{in}}$  associated with the in-coupling rate  $\rho_{\text{in}}$ : the higher  $\rho_{\text{in}}$  becomes, the larger does the stored/trapped bandwidth ( $\Delta\omega_{\text{in}}$ ) become. Therefore, this ( $\Delta\omega = \Delta\omega_{\text{in}}$ ) is the bandwidth that is stored/trapped in our asymmetric resonant system, assuming that  $\Delta\omega_{\text{in}}$  lies completely within the CUP region. The out-coupling bandwidth  $\Delta\omega_{\text{out}} (\approx 2\pi/\tau_0)$  is dependent on the material loss for the herein considered perfectly asymmetric case where  $\rho_{\text{out}} \rightarrow 0$ . While the loss spectrum can have a sharp resonance (in fact, one is required to achieve a low loss rate) this can be centered on a frequency far from the operating range, with a weak dependence of loss on frequency in the relevant frequency regime – see Fig. S2(C). Thus, in this nonreciprocal system, both, large storage times  $\Delta\tau = \tau_0$  (i.e., small out-coupling bandwidths  $\Delta\omega_{\text{out}} \approx 2\pi/\tau_0$  lost from the in-coupling bandwidth  $\Delta\omega_{\text{in}}$ ) and large bandwidths ( $\Delta\omega = \Delta\omega_{\text{in}}$  large for high  $\rho_{\text{in}}$ ) are simultaneously possible – whereas conventionally, for reciprocal systems,  $\Delta\tau$  and  $\Delta\omega$  are fundamentally reciprocal to one another.

To more clearly illustrate these, Fig. S2 below summarizes the spectrum of our pulse at various locations (i.e., at various/different time instances) as it is progressively trapped and stored into its trapping region at the terminated, rightmost end of the heterostructure (Fig. S2(A) below). One may clearly see from these results that the whole spectrum of the pulse is rigorously stored in its trapping region in this static, linear system – unlike, e.g., what one might have expected for time-varying or nonlinear resonant systems, in

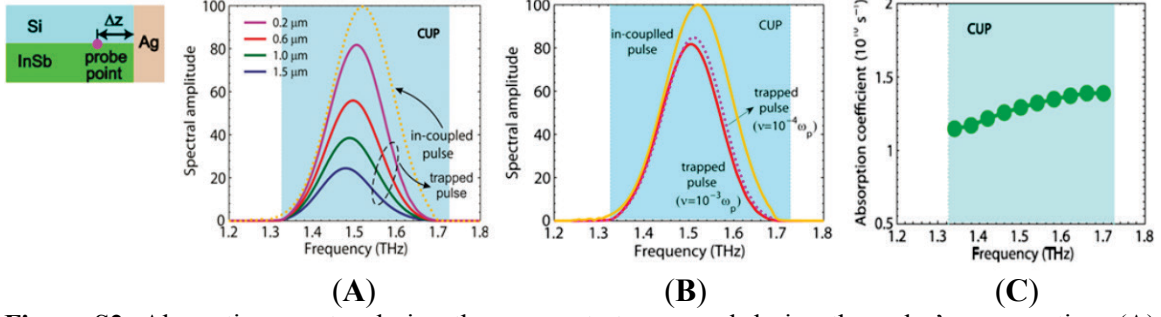


**Figure S2:** Absorption spectra during the resonant storage and during the pulse’s propagation. (A) Spectrum of trapped pulse at several points in the trapping region (cf. leftmost panel), and (B) for two different values of InSb loss factor  $\nu$ , at a point  $\Delta z = 0.2 \mu\text{m}$  (cf. leftmost panel) in both cases shown in (B). (C) Calculated from full-wave simulations optical losses within the ‘complete unidirectional propagation’ (CUP) band for  $\nu = 0.001\omega_p$ .

which case the spectrum would have been manipulated. The small redshift that we observe in the spectra of the stored pulse at various locations (time instances) in Fig. S2(A) is attributed to the slightly increased optical losses with frequency in our structure, as was calculated from full-wave simulations and is shown in Fig. S2(C) above. Likewise, Fig. S2(B) shows that the spectra of the trapped pulse remain unaffected when varying the InSb loss factor  $\nu$ , as expected, since as mentioned above the magnitude of the material losses cannot change the shape of the spectra (such a modification might have been caused, e.g., by a change in the dispersion / ‘slope’ of the material losses).

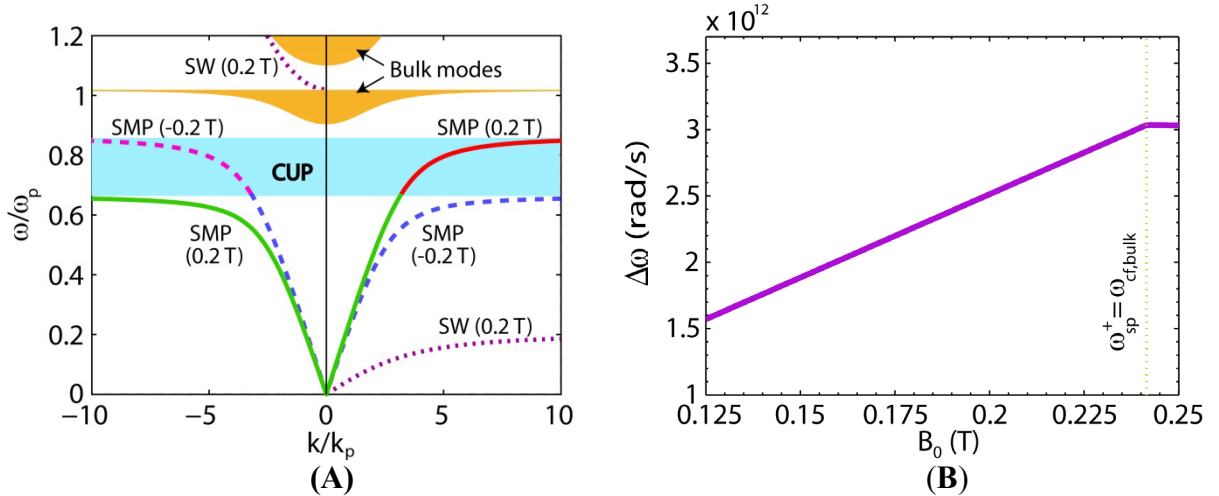


**Figure S3.** Bandstructure and bandwidth of the unidirectional-propagation region. (A) Band diagram of the heterostructure of Fig. 2B (cf. Fig. 2C), but now also shown is the case where a static magnetic bias  $B_0 = 0.2 \text{ T}$  is applied in the  $+\gamma$  direction. The curve corresponding to that case is shown with a dashed line. (B) Shown here is the blue solid line of Fig. 4C but now plotted on a linear scale, showing clearly the gradual increase of the structure’s bandwidth with increasing magnetic field  $B_0$  (cf. remarks immediately after Eq. (7)).



## References and Notes

1. E. I. Green, The story of *Q*. *Am. Sci.* **43**, 584–594 (1955).
2. K. S. Johnson, *Transmission Circuits for Telephonic Communication* (Western Electric, 1924).
3. A. E. Siegman, *Lasers* (Univ. Science Books, Sausalito, CA, 1986), pp. 105–108.
4. K. J. Vahala, Optical microcavities. *Nature* **424**, 839–846 (2003).  
[doi:10.1038/nature01939](https://doi.org/10.1038/nature01939) [Medline](#)
5. W. Ketterle, 8.421 Atomic and Optical Physics I, Spring 2014 (Massachusetts Institute of Technology: MIT OpenCourseWare, 2014), min. 1:09:00;  
<http://ocw.mit.edu/8-421S14>.
6. A. Papoulis, *Signal Analysis* (McGraw-Hill, 1977), sect. 8.2.
7. R. W. Boyd, D. J. Gauthier, A. L. Gaeta, A. E. Willner, Maximum time delay achievable on propagation through a slow-light medium. *Phys. Rev. A* **71**, 023801 (2005). [doi:10.1103/PhysRevA.71.023801](https://doi.org/10.1103/PhysRevA.71.023801)
8. P. W. Milonni, *Fast Light, Slow Light, and Left-Handed Light* (Institute of Physics Series in Optics and Optoelectronics, CRC Press, 2005).
9. J. B. Khurgin, R. S. Tucker Eds., *Slow Light: Science and Applications* (CRC Press, 2009).
10. R. W. Boyd, D. J. Gauthier, Controlling the velocity of light pulses. *Science* **326**, 1074–1077 (2009). [doi:10.1126/science.1170885](https://doi.org/10.1126/science.1170885) [Medline](#)
11. L. V. Hau, S. E. Harris, Z. Dutton, C. H. Behroozi, Light speed reduction to 17 metres per second in an ultracold atomic gas. *Nature* **397**, 594–598 (1999).  
[doi:10.1038/17561](https://doi.org/10.1038/17561)
12. M. D. Lukin, A. Imamoglu, Controlling photons using electromagnetically induced transparency. *Nature* **413**, 273–276 (2001). [doi:10.1038/35095000](https://doi.org/10.1038/35095000) [Medline](#)
13. D. A. B. Miller, Fundamental limit to linear one-dimensional slow light structures. *Phys. Rev. Lett.* **99**, 203903 (2007). [doi:10.1103/PhysRevLett.99.203903](https://doi.org/10.1103/PhysRevLett.99.203903) [Medline](#)
14. J. B. Khurgin, Slow light in various media: A tutorial. *Adv. Opt. Photonics* **2**, 287–318 (2010). [doi:10.1364/AOP.2.000287](https://doi.org/10.1364/AOP.2.000287)
15. Q. Xu, P. Dong, M. Lipson, Breaking the delay-bandwidth limit in a photonic structure. *Nat. Phys.* **3**, 406–410 (2007). [doi:10.1038/nphys600](https://doi.org/10.1038/nphys600)
16. L. Novotny, B. Hecht, *Principles of Nano-Optics* (Cambridge Univ. Press, 2012).
17. H. A. Haus, *Waves and Fields in Optoelectronics* (Prentice-Hall, 1984), chap. 7.
18. K. Vahala, *Optical Microcavities* (World Scientific, 2005).
19. See supplementary materials.
20. J. J. Brion, R. F. Wallis, A. Hartstein, E. Burstein, Theory of surface magnetoplasmons in semiconductors. *Phys. Rev. Lett.* **28**, 1455–1458 (1972).  
[doi:10.1103/PhysRevLett.28.1455](https://doi.org/10.1103/PhysRevLett.28.1455)

21. L. Shen, Y. You, Z. Wang, X. Deng, Backscattering-immune one-way surface magnetoplasmons at terahertz frequencies. *Opt. Express* **23**, 950–962 (2015). [doi:10.1364/OE.23.000950](https://doi.org/10.1364/OE.23.000950) [Medline](#)
22. D. Jalas, A. Petrov, M. Eich, W. Freude, S. Fan, Z. Yu, R. Baets, M. Popović, A. Melloni, J. D. Joannopoulos, M. Vanwolleghem, C. R. Doerr, H. Renner, What is – and what is not – an optical isolator. *Nat. Photonics* **7**, 579–582 (2013). [doi:10.1038/nphoton.2013.185](https://doi.org/10.1038/nphoton.2013.185)
23. D. M. Pozar, *Microwave Engineering* (Wiley, 2011).
24. S. M. Dutra, *Cavity Quantum Electrodynamics: The Strange Theory of Light in a Box* (Wiley, 2005), p. 34.
25. R. Zhang, S. R. Garner, L. V. Hau, Creation of long-term coherent optical memory via controlled nonlinear interactions in Bose-Einstein condensates. *Phys. Rev. Lett.* **103**, 233602 (2009). [doi:10.1103/PhysRevLett.103.233602](https://doi.org/10.1103/PhysRevLett.103.233602) [Medline](#)
26. J. Gómez Rivas, C. Janke, P. Bolivar, H. Kurz, Transmission of THz radiation through InSb gratings of subwavelength apertures. *Opt. Express* **13**, 847–859 (2005). [doi:10.1364/OPEX.13.000847](https://doi.org/10.1364/OPEX.13.000847) [Medline](#)
27. R. W. Boyd, Material slow light and structural slow light: Similarities and differences for nonlinear optics. *J. Opt. Soc. Am. B* **28**, A38–A44 (2011). [doi:10.1364/JOSAB.28.000A38](https://doi.org/10.1364/JOSAB.28.000A38)
28. W. H. Wee, J. B. Pendry, Universal evolution of perfect lenses. *Phys. Rev. Lett.* **106**, 165503 (2011). [doi:10.1103/PhysRevLett.106.165503](https://doi.org/10.1103/PhysRevLett.106.165503) [Medline](#)
29. U. Leonhardt, T. Tyc, Broadband invisibility by non-Euclidean cloaking. *Science* **323**, 110–112 (2009). [doi:10.1126/science.1166332](https://doi.org/10.1126/science.1166332) [Medline](#)
30. F. Monticone, A. Alù, Invisibility exposed: Physical bounds on passive cloaking. *Optica* **3**, 718–724 (2016). [doi:10.1364/OPTICA.3.000718](https://doi.org/10.1364/OPTICA.3.000718)
31. C. E. Rüter, K. G. Makris, R. El-Ganainy, D. N. Christodoulides, M. Segev, D. Kip, Observation of parity-time symmetry in optics. *Nat. Phys.* **6**, 192–195 (2010). [doi:10.1038/nphys1515](https://doi.org/10.1038/nphys1515)
32. M. Z. Hasan, C. L. Kane, *Colloquium*: Topological insulators. *Rev. Mod. Phys.* **82**, 3045–3067 (2010). [doi:10.1103/RevModPhys.82.3045](https://doi.org/10.1103/RevModPhys.82.3045)
33. M. C. Rechtsman, J. M. Zeuner, Y. Plotnik, Y. Lumer, D. Podolsky, F. Dreisow, S. Nolte, M. Segev, A. Szameit, Photonic Floquet topological insulators. *Nature* **496**, 196–200 (2013). [doi:10.1038/nature12066](https://doi.org/10.1038/nature12066) [Medline](#)
34. A. B. Khanikaev, S. H. Mousavi, W.-K. Tse, M. Kargarian, A. H. MacDonald, G. Shvets, Photonic topological insulators. *Nat. Mater.* **12**, 233–239 (2013). [doi:10.1038/nmat3520](https://doi.org/10.1038/nmat3520) [Medline](#)